Spectroscopic Signatures for Interlayer Coupling in MoS_2–WSe_2 van der Waals Stacking

Ming-Hui Chiu,[†,⊗] Ming-Yang Li,[‡,⊗] Wengjing Zhang,[§,⊥] Wei-Ting Hsu,[∥] Wen-Hao Chang,[∥] Mauricio Terrones,[#] Humberto Terrones,[▽] and Lain-Jong Li*[,†]

[†]Physical Sciences and Engineering, King Abdullah University of Science and Technology, Thuwal 23955-6900, Kingdom of Saudi Arabia, [‡]Institute of Atomic and Molecular Sciences, Academia Sinica, Taipei 11529, Taiwan, [§]Department of Physics, National University of Singapore, 2 Science Drive 3, Singapore 117542, [⊥]SZU-NUS Collaborative Innovation Center for Optoelectronic Science & Technology, Shenzhen University, Shenzhen 518060, China, [∥]Department of Electrophysics, National Chiao Tung University, Hsinchu 300, Taiwan, [#]Department of Physics, Chemistry, Materials Science and Engineering and Center for 2-Dimensional and Layered Materials, The Pennsylvania State University, 104 Davey Lab., University Park, Pennsylvania 16802, United States, and [▽]Departament of Physics, Applied Physics and Astronomy, Rensselaer Polytechnic Institute, 110 Eighth Street, Troy, New York 12180, United States. [⊗]These authors contributed equally.

ABSTRACT Stacking of MoS_2 and WSe_2 monolayers is conducted by transferring triangular MoS_2 monolayers on top of WSe_2 monolayers, all grown by chemical vapor deposition (CVD). Raman spectroscopy and photoluminescence (PL) studies reveal that these mechanically stacked monolayers are not closely coupled, but after a thermal treatment at 300 °C, it is possible to produce van der Waals solids consisting of two interacting transition metal dichalcogenide (TMD) monolayers. The layer-number sensitive Raman out-of-plane mode A^2_{1g} for WSe_2 (309 cm^{-1}) is found sensitive to the coupling between two TMD monolayers. The presence of interlayer excitonic emissions and the changes in other intrinsic Raman modes such as E″ for MoS_2 at 286 cm^{-1} and A^2_{1g} for MoS_2 at around 463 cm^{-1} confirm the enhancement of the interlayer coupling.

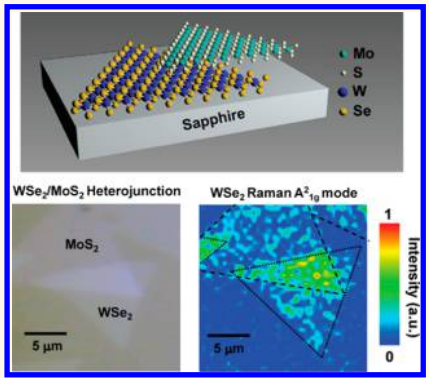

KEYWORDS: transition metal dichalcogenides · tungsten diselenides · molybdenum disulfide · van der Wall stacking · heterojunction · interlayer coupling

Semiconducting transition metal dichalcogenide (STMD) layered materials exhibit unique layer-dependent electronic and optical properties.[1−12] For example, molybdenum disulfide (MoS_2) exhibits an indirect bandgap of 1.2 eV in bulk, but it becomes a direct gap semiconductor (bandgap = 1.8 eV) when thinned to a monolayer.[4,8] Hence, monolayer MoS_2 transistors have been fabricated and these devices have showed excellent current on/off ratios.[10−12] MoS_2 is known as an *n*-type semiconductor due to the presence of S vacancies. Another STMD, tungsten diselenide (WSe_2), has just started to attract the attention of numerous scientists due to its p-type characteristics.[2,13] In addition to the mechanical exfoliation method to prepare STMD layers, recent developments in the scalable synthesis of STMD monolayers using chemical vapor deposition (CVD) opened up the possibility to form large area of STMD monolayers that could result in fabrication of flexible electronic devices and photodetectors.[1,2,14] Furthermore, it is also possible to envisage building unprecedented solids by stacking monolayers of different 2-D systems one on top of another (*e.g.*, TMDs, h-BN and graphene).[15−21] Such stacked heterostructures based on atomically thin 2D layers are fundamentally different since only van der Waals interactions exist at the interfaces. Therefore, these layered materials (termed also van der Waals solids) enable the preparation of high-quality heterointerfaces without the need of fulfilling an atomic commensurability,[17,18,22] thus making the structure construction easily achievable. Very recently, $MoSe_2$/WSe_2 optical studies were performed,[23] and other optoelectronic devices based on WSe_2/MoS_2 *p*–*n* junction were also proposed.[24−27] Interestingly, the gate-tunable diode-like current rectification and a photovoltaic response have been recently observed in WSe_2/MoS_2 heterojunctions.[24−26] It should be noted that the optical

* Address correspondence to lance.li@kaust.edu.sa.

Received for review July 30, 2014 and accepted September 7, 2014.

Published online September 07, 2014
10.1021/nn504229z

and electrical properties of TMD heterojuctions strongly depend on the interaction among layers, and efforts aiming at elucidating their proper characterization is currently underway.

In this paper, we demonstrate that it is possible to build van der Waals solids by first stacking CVD-grown MoS_2 on WSe_2 monolayers, followed by thermal annealing. The layer-number sensitive Raman mode A^2_{1g} for WSe_2 at around 309 cm^{-1} (out-of-plane mode) appears to be excellent parameters when evaluating a good coupling between monolayers. The Raman modes for bulk MoS_2 at *ca.* 463 cm^{-1} (A^2_{1g}) and at *ca.* 283 cm^{-1} (E″) are also enhanced by interlayer coupling. In addition, the interlayer excitonic peak observed in photoluminescence (PL) confirms the coupling between two TMD monolayers and a band diagram of the MoS_2/WSe_2 heterojunction and the exciton binding energies for each composition are proposed.

RESULTS AND DISCUSSION

Preparation and Characterizations of Heterojunction. Triangular WSe_2 and MoS_2 single crystalline monolayers with the lateral dimension of few tens of micrometers were synthesized on c-plane sapphire substrates by CVD.[1,2] In brief, transition metal trioxides (MoO_3 or WO_3) were vaporized and reacted with the S or Se vapor in a hot-wall furnace under a controlled gaseous environment to form MoS_2 or WSe_2 monolayers (see details in Methods). To build a van der Waals solid (or vertical heterojunction of MoS_2 on WSe_2), as schematically illustrated in Figure 1a, we first detached as-synthesized MoS_2 triangular islands using PMMA. In particular, a layer of PMMA was spin-coated on MoS_2 followed by dipping it in NaOH so as to release the PMMA-supported MoS_2 from the substrates. The PMMA supported-MoS_2 was then mechanically transferred onto WSe_2 flakes followed by the removal/cleaning of PMMA.[3] Figure 1b is the optical micrograph (OM) showing the mechanically stacked MoS_2/WSe_2 monolayers, in which it is possible to distinguish the stacked layers by noticing a color contrast. Supporting Information Figure S1 shows the atomic force microscopy (AFM) image of as-transferred MoS_2/WSe_2, where the surface of the sample is covered with residuals and adsorbates. In this context, it has been demonstrated by scanning tunneling microscopy (STM) that the majority of the adsorbates and residuals can be removed after thermal annealing at elevated temperatures.[28] Therefore, as-prepared MoS_2/WSe_2 samples were then annealed in an hydrogen/Ar environment (atmosphere pressure; H_2:Ar = 1:4) at 300 °C for 4 h. The detailed fabrication process is described in Methods.

The AFM image and cross-sectional profile of the MoS_2/WSe_2 heterojunction are shown in Figure 1c, demonstrating that both WSe_2 and MoS_2 are indeed monolayers (thickness for each is around 0.6−0.7 nm). The AFM image also shows that the individual flakes

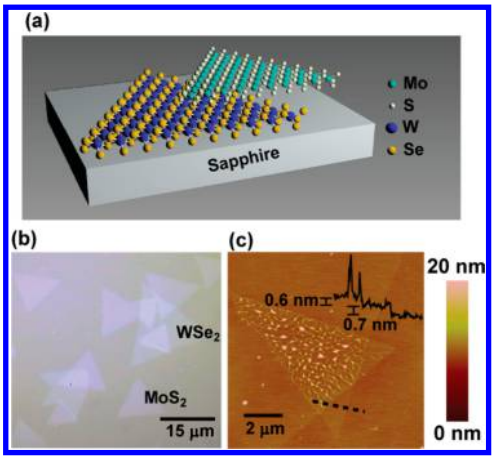

Figure 1. Representation of the vertical heterojunction consisting of MoS_2 monolayers deposited on top of WSe_2 monolayers: (a) schematic illustration of the MoS_2/WSe_2 van der Waals heterojunction; (b) optical micrograph of the mechanically stacked MoS_2/WSe_2 structure after thermal annealing, and (c) AFM image of the MoS_2/WSe_2 heterojunction. The cross-sectional height profile along the dashed line indicates that each layer is about 0.6−0.7 nm in thickness.

are clean and without cracks or holes after the H_2/Ar thermal treatment. Interestingly, the corrugated structures are found at the overlapped region, which could be due to a commensurability adjustment of the layers in order to minimize the energy followed the thermal treatment. Alternatively, it is also possible that water, used as the solvent to transfer MoS_2 onto WSe_2, got trapped between MoS_2 and WSe_2 monolayers, and its evaporation resulted in the corrugation of the top transferred layer during the thermal treatment. The high spikes of the cross-sectional profile in inset of Figure 1c reveal the profile of the corrugated structures.

Raman Features. For the Raman spectra we have used the notation of the monolayer modes using the symbols A'_1, E′, and the notation of the bilayer for the higher order out of plane modes such as the A^2_{1g}, since these modes are not Raman active in the monolayer. Figure 2a−d shows the Raman spectra of the double layer van der Waals solid excited with a 473 nm laser in four energy regions, where the curves from the top to bottom are MoS_2 region (blue), MoS_2/WSe_2 heterojunction before annealing (green; μM/W), MoS_2/WSe_2 heterojunction after annealing (red; cM/W), and WSe_2 region (black), respectively. The characteristic peaks for WSe_2 at about 250 cm^{-1} (E′ and A'_1 degenerated mode) and those for MoS_2 located at 387 cm^{-1} (E′ mode; in-plane vibration) and 402 cm^{-1} (A'_1 mode; out-of-plane vibration) are observed in individual monolayers of WSe_2 and MoS_2. In addition, the layer-number sensitive mode A^2_{1g} for WSe_2 at around 309 cm^{-1} (out-of-plane mode) has been reported only observable when the WSe_2 is a bilayer or thicker.[29,30] A similar feature A^2_{1g} for bulk MoS_2 is located at around 463 cm^{-1}.[31−36] Furthermore, there is another characteristic peak for bulk MoS_2 at around 284 cm^{-1} in odd number of layers

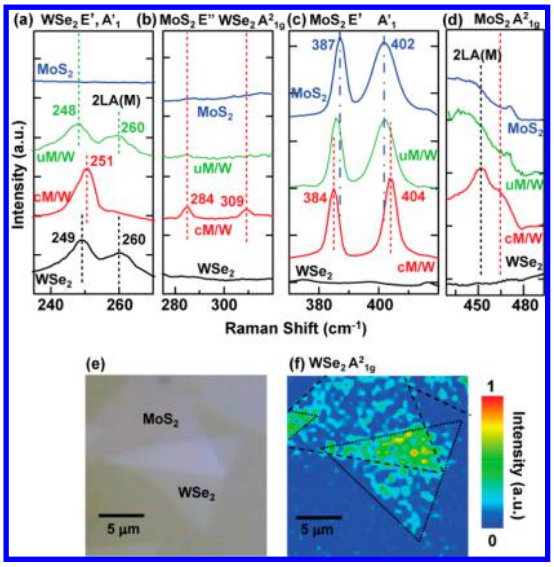

Figure 2. Raman spectra of the MoS_2/WSe_2 heterojunction. (a–d) Raman spectra for MoS_2 (blue), uncoupled MoS_2/WSe_2 heterojunction (green; μM/W), coupled MoS_2/WSe_2 heterojunction (red; cM/W), and WSe_2 (black) from the top to the bottom plot. The curves are shifted for clarity. (e) Optical microscopic image for the MoS_2/WSe_2 heterojunction. (f) The spatial mapping of the Raman intensity for WSe_2 A^2_{1g} peak in the selected area shown in (e).

is called E″ and in even number of layers becomes E_g due to the symmetry involved.[31−33] Our Raman results for either MoS_2 or WSe_2 region do not exhibit these characteristic peaks, confirming that WSe_2 and MoS_2 are monolayers. Note that the Raman band at 260 cm^{-1} observed at WSe_2 region (Figure 2a) and at about 450 cm^{-1} at MoS_2 region (Figure 2d) corresponds to the second order LA(M) phonon (2LA(M)).[35−37]

It is observed that the Raman peaks for either MoS_2 or WSe_2 region show no obvious change after the thermal annealing at 300 °C as shown in Supporting Information Figure S2a, which implies that the annealing process does not cause significant structural defects or modification. For the heterojunction before annealing, we find that the Raman characteristic peaks are closely coinciding with the individual WSe_2 and MoS_2 regions, which implies that the layers are uncoupled (independent from each other). By contrast, after the thermal annealing process, the Raman spectrum for the heterojunction becomes significantly different from that for the individual WSe_2 and MoS_2 monolayers. First, the layer-sensitive characteristic peak A^2_{1g} for WSe_2 at 309 cm^{-1} clearly appear in Figure 2b. Second, the E′ and A'_1 degenerated peak for the WSe_2 shows a blue-shift as shown in Figure 2a, and the A'_1 (E′) for the MoS_2 shows blue (red)-shifts as shown in Figure 2c, respectively. Third, the anomaly E″ feature for MoS_2 is also observed in Figure 2b, and the layer-sensitive peak A^2_{1g} for MoS_2 is enhanced as found in Figure 2d.

The presence of the layer-sensitive Raman bands after thermal annealing strongly evidence that the

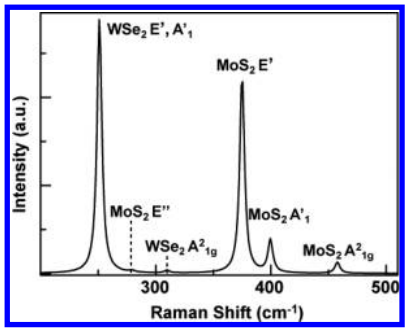

Figure 3. Raman scattering modes simulation of the MoS_2/WSe_2 heterojunction.

MoS_2 and WSe_2 interact with each other. It is also possible that some contaminants such as adsorbates trapped between MoS_2 and WSe_2 weaken the coupling between these two layers. After the thermal treatment, these contaminants are efficiently removed (as indicated by AFM), thus resulting in the commensurate stacking and the shifts in the Raman peaks. Figure 2e is the OM for the selected area for Raman mapping studies. Figure 2f shows the spatial mappings for the peak intensity of the Raman bilayer signature at 309 cm^{-1} for WSe_2 A^2_{1g} mode, and the Raman features is only observed and distributed uniformly in the stacked region, indicating that the peak is originated from the interlayer coupling in the new MoS_2/WSe_2 bilayer. It is noteworthy that the peak A^2_{1g} is Raman inactive in monolayer but become active in homobilayer or thicker layers. Here, the heterojunction stacking likely introduces a similar effect as in stacked homolayers, leading to the symmetry change and activation of the Raman features.

To further investigate the main features observed in the experimental Raman spectra of the MoS_2/WSe_2 junction, density functional theory (DFT) and density functional perturbation theory (DFPT) calculations were carried out using the plane wave code CASTEP as implemented in the Materials Studio package.[38] A hexagonal unit cell with one layer of MoS_2 and another of WSe_2 arranged in an AB stacking was considered under the local density approximation (LDA). To provide a reasonable description of the van der Waals interaction, we have considered a dispersion correction for LDA (LDA-D).[39] After the relaxation, due to the lattice mismatch between the monolayers, the MoS_2 lattice parameter suffered an expansion from 3.16 to 3.21 Å and the WSe_2 lattice contracted from 3.28 to 3.21 Å. The phonon dispersion and Raman scattering modes were calculated using the linear response approach for insulators.[40] The result of Raman scattering modes is shown in Figure 3, where all the modes, not the resonant second order or combinations of first order modes, are shown in the Figure 3. The characteristic peaks E′ and A'_1 for WSe_2 and MoS_2 are exactly reproduced. The MoS_2/WSe_2 bilayer vibrations at 309 cm^{-1} (WSe_2 A^2_{1g}) is also clearly seen from

the simulation. Although the calculated frequencies are not exactly the same as obtained in experiments, the simulation results provide a good approximation of the Raman signals observed. The coincidence between the experimental and simulated results implies that the coupling exists in the MoS_2/WSe_2 bilayer heterojunction.

The Raman simulation in Figure 3 also presents the MoS_2 bulk vibration mode A^2_{1g} at 458 cm^{-1} and the anomaly E″ mode at 279 cm^{-1}. Comparing to our experimental results, although there have other Raman active modes near 460 cm^{-1}, the MoS_2 A^2_{1g} mode still can be identified in Figure 2d for cW/M sample. The observed E″ mode at 284 cm^{-1} in Figure 2b for cW/M sample can also be correlated to the simulation result. This peak is not normally observed because of the Raman geometry used (backscattering geometry) and also because it has low intensity. The observation on the E″ mode may indicate that the presence of the interlayer coupling could enhance its intensity. The observation on these Raman peaks for bulk MoS_2 is also an evidence of the existence of the interlayer coupling between MoS_2 and WSe_2.

It is known that the Raman E′ peak of monolayer MoS_2 is sensitive to strain and strain could induce a red-shift in the E′ modes that have been observed for MoS_2 monolayer or multilayers in other reports.[33,41−43] The red-shift of the MoS_2 E′ peak after the two layers are coupled (thermally treated) shown in Figure 2c indicates that a tensile strain has been imposed to the MoS_2. This also implies that the WSe_2 monolayer experiences a compressive strain and the E′ peak of WSe_2 also shows an opposite blue-shift as shown in Figure 2a. As stated above, our simulation concludes the expansion of the MoS_2 and contraction of the WSe_2 (details in Methods) which explain in part the E′ peak shift in MoS_2 and WSe_2 after the two layers are coupled.

Although the strain effect could explain the Raman shifts of the annealed hetero bilayer, we still cannot exclude the possibility of charge transfer between these stacked layers. The Raman A'_1 peak of MoS_2 blue-shifts and its intensity increases (relative to E′), thus indicating that MoS_2 is less n-doped (or a decrease in the electron concentration).[44,45] The blue-shift of the WSe_2 Raman A'_1 peak implies that the WSe_2 may become less p-doped (Supporting Information Figure S3 shows that in our separate experiment, p-doping from $AuCl_4^-$ causes a red-shift of Raman A'_1 peak in monolayer WSe_2). These phenomena suggest that the electrons transfer from MoS_2 to WSe_2, which is expected for the PN-junction composed by the p-type WSe_2 and n-type MoS_2.[24−27] It is also noted that the effect of a compressive strain on E′ and the n-doping effect on A'_1 in WSe_2 is not easily distinguishable since A'_1 and E′ frequencies in WSe_2 are degenerate and both effects are expected to cause the blue-shift. However, the fact that the Raman shift of MoS_2 E′ mode is larger than the A'_1 mode implies that the strain effect should play a major role than doping effect. On the other hand, the theoretical simulation including only the strain relaxation can well reproduce our experimental results, which further suggests that the strain effect is more significant. In any case, the shifts indicate the interaction between two stacked heterolayers. It is worth noting that our results show that the A'_1 and E′ peak energies of MoS_2 do not seem to depend on the stacking angle between the two layers as shown in Supporting Information Figure S4, which is different from the recent studies on Raman spectra of bilayer MoS_2 which shows twisting angle dependence.[46,47] This could be reasoned since the homobilayer might exhibit stronger interlayer coupling due to the same lattice constant for two layers (better matching between top and bottom layers).

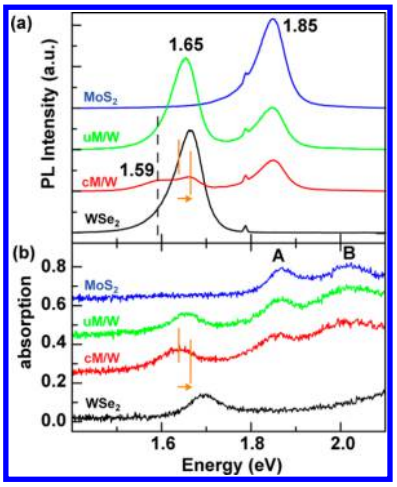

Figure 4. (a) Photoluminescence and (b) absorption spectroscopy of the MoS_2/WSe_2 heterojunction. The curves corresponding to MoS_2 (blue), noncoupled MoS_2/WSe_2 heterojunction (μM/W) (green), coupled MoS_2/WSe_2 heterojunction (cM/W) (red), and WSe_2 (black) from up to down. The curves are shifted for clarity. The dashed line indicates the interlayer PL peak. The orange lines and arrow mark the anti-Stoke shift.

Band Gaps and Band Alignments. To study the optical and energy band properties of the heterojunction, we performed the PL and absorption measurements. Figure 4a shows the PL spectra excited with a 532 nm laser and Figure 4b displays the absorption spectra for MoS_2, uncoupled MoS_2/WSe_2 heterojunction (μM/W), coupled MoS_2/WSe_2 heterojunction (cM/W), and WSe_2 regions. The excitonic PL peaks for WSe_2 and MoS_2 monolayers at about 1.65 and 1.85 eV are clearly observed in the respective nonstacking region, and the peak energies also hold after annealing process as shown in Supporting Information Figure S2b. For the μM/W region, the PL peak energy of WSe_2 or MoS_2 is very close to that for its corresponding layer, thus confirming that there is no strong layer coupling in the heterojunction. The slight suppression of the PL intensity for both MoS_2 and WSe_2 may be due to the

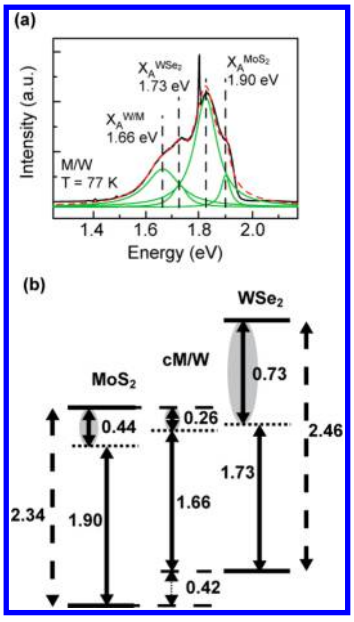

Figure 5. Schematic of the energy band alignment of MoS_2/WSe_2 heterojunction at 77 K. (a) The PL of cM/W sample (black) and the Lorentzian peaks fitting (red-dashed) at 77 K. The green lines are the composited peaks by using Lorentzian fitting. The black dashed lines indicate the emitted energy of MoS_2 and WSe_2 and cM/W. (b) The solid lines represent the conduction band and valence band of MoS_2 and WSe_2. The solid double arrow lines, dashed double arrow lines, and dot double arrow lines indicate the PL energy, band gap energy, and the valence band offset between MoS_2 and WSe_2 extracted from experimental results, respectively. The solid double arrow lines with gray background indicate the derived exciton binding energy.

defects/traps introduced by the stacking. For the cM/W sample, the PL intensity for both WSe_2 and MoS_2 is significantly lower compared to that of uM/W. In addition to the characteristic PL peaks from MoS_2 and WSe_2, an extra peak at a lower energy (~1.59 eV), and marked by a black dashed line is also observed. This PL peak appeared in previous work and it is attributed to the interlayer radiative recombination of the spatially separated carriers.[27] The excitons are excited separately in WSe_2 and MoS_2 by the incident laser. Since the MoS_2/WSe_2 junction is a type II heterojunction, the excited electrons in WSe_2 tend to accumulate in the conduction band of MoS_2 and the holes in MoS_2 in the valence band of WSe_2 at the interface as illustrated in Figure 5b. Therefore, the recombination of the electron–hole pairs at the interface gives lower energy than MoS_2 and WSe_2 itself. The interlayer PL peak reveals the nature of the coupling in the heterojunction.

The absorption spectrum for individual MoS_2 exhibits two absorptions peaks, A and B excitonic peaks at 1.87 and 2.01 eV, respectively. The WSe_2 has only one peak centered at 1.70 eV. As shown in Figure 4b, the absorption peak of the pristine WSe_2 is significantly higher (50–60 meV) than that of either μW/M or cW/M, which might be due to that the WSe_2 is under MoS_2 and the dielectric environment is largely changed. Moreover, a Stoke shift is found in cM/W sample between absorption peak (1.64 eV) and interlayer PL peak (1.59 eV), which further supports the radiative recombination between the WSe_2 and MoS_2. We should note that we found an anti-Stoke shift in the cM/W sample between the WSe_2 absorption peak (1.64 eV) and WSe_2 PL peak (1.66 eV), as marked with orange lines in Figure 4. The anti-Stoke shift implies that there might have some hot phonons in the optical level of WSe_2 under the heterojunction structure, which requires further experiments and theoretical work to clarify.

The observation on the interlayer PL peak not only show the strong evidence of the interlayer coupling, but also allow us to establish the energy band alignment of the MoS_2/WSe_2 heterojunction and the exciton binding energy of the junction as shown in Figure 5b. According to our previous work on STS[28] and μ-XPS,[48] we know that the energy band gaps for MoS_2 and WSe_2 are 2.34 and 2.46 eV, respectively, and the valence band offset is 0.42 eV. For consistency, we measure the PL spectrum at 77K to set the energy band alignment. The PL spectrum at 77 K for each regime is shown in Figure 5a, and the extracted PL peaks are summarized in Figure 5b with solid double arrow lines. On the basis of these, we can determine the binding energy of the MoS_2/WSe_2 interlayer exciton, as marked by solid double arrow line with gray background, to clarify the discrepancy raised form previous works.[49−52] We find that the MoS_2/WSe_2 interlayer exciton has a lower exciton binding energy 0.26 eV when compared to MoS_2 or WSe_2. The band alignment reveals the important role of the interlayer coupling, which is crucial for band engineering. In our work, we confirmed that the annealing process can enhance the interlayer coupling, which might result from reducing of layer distance or exclusion of interface residues in order to build van der Waals solids. Besides, we have also performed the experiments for the opposite stacking structure (WSe_2 on top of MoS_2) and this structure exhibits the similar behaviors in Raman (Supporting Information Figure S5) and PL (Supporting Information Figure S6), further corroborating the conclusions reached.

CONCLUSIONS

We fabricated the vertical MoS_2/WSe_2 heterojunction by stacking CVD-grown MoS_2 and WSe_2 triangular monolayers. The thermal treatment enhances the coupling between the two monolayers, based on the shifts observed in the Raman and PL spectra. Interestingly, the characteristic Raman signature at 309 cm^{-1} (WSe_2 A^2_{1g}), 463 cm^{-1} (MoS_2 A^2_{1g}), and 286 cm^{-1} (MoS_2 E'') suggest that the heterostructural stacking impose similar symmetry change as homostructural stacking. Together with the reported STS and μ-XPS results, the energy band alignment of the MoS_2/WSe_2 heterojunction and the

exciton binding energy were established. It is anticipated that the fundamental understanding of interlayer coupling and the band alignments in heterostructures is crucially important for future applications and engineering of the devices based on two-dimensional materials and van der Waals solids.

METHODS

WSe_2/MoS_2 Monolayer Single Crystal Growth. WSe_2 and MoS_2 monolayer single crystal were separately growth by chemical vapor deposit method. The WO_3/MoO_3 powders (0.3/0.6 g) were placed in a quartz boat located in the heating zone center of the furnace. The Se/S powders were placed in a separate quartz boat at the upper stream side of the furnace and the temperature was maintained at 290/170 °C during the reaction. The sapphire substrates for growing were put at the downstream side, next to quartz boat. The gas flow was brought by an $Ar/H_2/Ar$ flowing gas (Ar = 90 sccm, H_2 = 10 sccm/Ar = 70 sccm), and the chamber pressure was controlled at 7/40 Torr. The center heating zone was heated to 925/635 °C. After reaching growth temperature, the heating zone was kept for 15/30 min and the furnace was then naturally cooled down to room temperature.

Heterojunction Fabrication. MoS_2 on sapphire substrate was spin-coated with PMMA (950 K), and then heated on hot plate at 100 °C for 20 min. The sample was then tipped into NaOH (2 M) solution and kept at 100 °C for 1 h. After sapphire-etching by NaOH, MoS_2 with PMMA film was transferred into DI water twice, each step for 10 min, to dilute NaOH etching solution. And then MoS_2 with PMMA was transferred on sapphire with WSe_2 and heating at 100 °C on hot plate for 30 min to evaporate the water at the interface. Following, the sample was put into acetone at 60 °C for 30 min to remove the PMMA. Finally, the sample was rinsed with IPA and water, and dried with N_2 gas. Before annealing, the samples were examined by AFM, Raman spectroscopy, PL, and absorption spectroscopy. The as-prepared MoS_2/WSe_2 samples were then annealed in an hydrogen/Ar environment (atmosphere pressure; H_2:Ar = 1:4) at 300 °C for 4 h. The annealing temperature was selected at 300 °C to effectively remove the residuals but not too high to initiate the formation of alloys such as MoS_xSe_y or WS_xSe_y.[53]

Characterizations. The AFM images were performed in a Veeco Dimension-Icon system. Raman spectra were collected in a confocal Raman system (NT-MDT). The wavelength of laser is 473 nm (2.63 eV), and the spot size of the laser beam is ~0.5 μm and the spectral resolution is 1 cm^{-1} (obtained with a 1800 grooves/mm grating). The PL and differential reflectance spectra were measured in a homemade microscopy system. For room-temperature PL measurements, a 532 nm solid-state laser was focused to a spot size <1 μm on the sample by an objective lens (×100; N.A. = 0.9). The PL signals were then collected by the same objective lens, analyzed by a 0.75 m monochromator and detected by a liquid-nitrogen-cooled CCD camera. The apparatus for the differential reflectance measurements are basically the same, except that the light source was replaced by a fiber-coupled tungsten-halogen lamp. For low-temperature PL measurements, the sample was cooled down to T = 10.8 K in a low-vibration cryogen-free cryostat. The objective lens for low-temperature measurements is a long working distance objective lens with N.A. = 0.42.

Phonon Dispersion and Raman Scattering Modes Simulation. The density functional theory (DFT) and density functional perturbation theory (DFPT) calculations were carried using the plane wave code CASTEP[38] as implemented in the Materials Studio package. A hexagonal unit cell with one layer of MoS_2 and another of WSe_2 arranged in a AB stacking (similar to the one observed in bulk crystals of trigonal prismatic transition metal dichalcogenides) was considered under the local density approximation (LDA) using the Ceperly-Alder-Perdew and Zunger (CA-PZ) functional[54,55] with 6X6X3 Monkhorst-Pack K-points and a plane waves cut off of 720 eV with a norm-conserving pseudopotential. The structure was relaxed, including the cell, until the forces became smaller than 0.01 eV/Å and with self-consistent energy tolerances less than 5×10^{-7} eV/atom. A vacuum of 16 Å between the cells was considered. The electronic structure results obtained for the individual layers and bulk are in agreement with those reported by other groups within the LDA formalism.[56,57] To provide a reasonable description of the van der Waals interaction, we have considered a dispersion correction for both LDA (LDA-D)[39] and for general gradient approximation (GGA-PW91)[58] finding that LDA provides a better description for the interlayer distance than LDA-D and corrected GGA-PW91, as described in a previous publications.[35,59] The phonon dispersion and Raman scattering modes were calculated using the linear response approach for insulators.[40] After the relaxation, due to the lattice mismatch between the monolayers, the MoS_2 lattice parameter suffered an expansion from 3.16 to 3.21 Å and the WSe_2 lattice contracted from 3.28 to 3.21 Å. The expansion of the MoS_2 and contraction of the WSe_2 explain in part the shifts in some of the modes found in the Raman signal due to strain. Nevertheless, the results obtained here provide a good approximation of the Raman signal observed.

Conflict of Interest: The authors declare no competing financial interest.

Acknowledgment. This research was partly supported by National Science Council Taiwan (NSC-102-2119-M-001-005-MY3 and NSC101-2628-M-009-002-MY3) and AFOSR BRI. W.-H.C. acknowledges the supports from the Center for Interdisciplinary Science under the MOE-ATU project for NCTU. M.-H.C. and L.-J.L. acknowledge the support from KAUST. M.T. acknowledges support by the U.S. Army Research Office under MURI ALNOS project, contract/grant number W911NF-11-1-0362, the Penn State Center for Nanoscale Science (seed grant on 2D Layered Materials -DMR-0820404), and the Center for 2-Dimensional and Layered Materials at The Pennsylvania State University.

Supporting Information Available: AFM image for the stacked area of the as-transferred MoS_2/WSe_2 sample; Raman and PL spectra for the WSe_2 and MoS_2 areas before and after annealing process; schematics and AFM images of the WSe_2 triangular flake after the doping process of immersion in a $AuCl^-_4$ solution; extracted peak positions of Raman A'_1 mode (upper) and E′ mode of MoS_2 with twist angle between MoS_2 and WSe_2; Raman and PL spectra of the WSe_2/MoS_2 heterojunction. This material is available free of charge *via* the Internet at http://pubs.acs.org.

REFERENCES AND NOTES

1. Lee, Y.-H.; Zhang, X.-Q.; Zhang, W.; Chang, M.-T.; Lin, C.-T.; Chang, K.-D.; Yu, Y.-C.; Wang, J. T.-W.; Chang, C.-S.; Li, L.-J.; *et al.* Synthesis of Large-Area MoS_2 Atomic Layers with Chemical Vapor Deposition. *Adv. Mater.* **2012**, *24*, 2320–2325.
2. Huang, J.-K.; Pu, J.; Hsu, C.-L.; Chiu, M.-H.; Juang, Z.-Y.; Chang, Y.-H.; Chang, W.-H.; Iwasa, Y.; Takenobu, T.; Li, L.-J. Large-Area Synthesis of Highly Crystalline WSe_2 Monolayers and Device Applications. *ACS Nano* **2013**, *8*, 923–930.
3. Lin, Y.-C.; Zhang, W.; Huang, J.-K.; Liu, K.-K.; Lee, Y.-H.; Liang, C.-T.; Chu, C.-W.; Li, L.-J. Wafer-Scale MoS_2 Thin Layers Prepared by MoO_3 Sulfurization. *Nanoscale* **2012**, *4*, 6637–6641.
4. Mak, K. F.; Lee, C.; Hone, J.; Shan, J.; Heinz, T. F. Atomically Thin MoS_2: A New Direct-Gap Semiconductor. *Phys. Rev. Lett.* **2010**, *105*, 136805.
5. Ramasubramaniam, A. Large Excitonic Effects in Monolayers of Molybdenum and Tungsten Dichalcogenides. *Phys. Rev. B* **2012**, *86*, 115409.
6. Lee, C.; Yan, H.; Brus, L. E.; Heinz, T. F.; Hone, J.; Ryu, S. Anomalous Lattice Vibrations of Single- and Few-Layer MoS_2. *ACS Nano* **2010**, *4*, 2695–2700.

7. Jones, A. M.; Yu, H.; Ghimire, N. J.; Wu, S.; Aivazian, G.; Ross, J. S.; Zhao, B.; Yan, J.; Mandrus, D. G.; Xiao, D.; *et al.* Optical Generation of Excitonic Valley Coherence in Monolayer WSe_2. *Nat. Nanotechnol.* **2013**, *8*, 634–638.
8. Splendiani, A.; Sun, L.; Zhang, Y.; Li, T.; Kim, J.; Chim, C.-Y.; Galli, G.; Wang, F. Emerging Photoluminescence in Monolayer MoS_2. *Nano Lett.* **2010**, *10*, 1271–1275.
9. Wang, Q. H.; Kalantar-Zadeh, K.; Kis, A.; Coleman, J. N.; Strano, M. S. Electronics and Optoelectronics of Two-dimensional Transition Metal Dichalcogenides. *Nat. Nanotechnol.* **2012**, *7*, 699–712.
10. Wang, H.; Yu, L.; Lee, Y.-H.; Shi, Y.; Hsu, A.; Chin, M. L.; Li, L.-J.; Dubey, M.; Kong, J.; Palacios, T. Integrated Circuits Based on Bilayer MoS_2 Transistors. *Nano Lett.* **2012**, *12*, 4674–4680.
11. Radisavljevic, B.; Radenovic, A.; Brivio, J.; Giacometti, V.; Kis, A. Single-Layer MoS_2 Transistors. *Nat. Nanotechnol.* **2011**, *6*, 147–150.
12. Radisavljevic, B.; Whitwick, M. B.; Kis, A. Small-Signal Amplifier Based on Single-Layer MoS_2. *Appl. Phys. Lett.* **2012**, *101*, 043103.
13. Fang, H.; Chuang, S.; Chang, T. C.; Takei, K.; Takahashi, T.; Javey, A. High-Performance Single Layered WSe_2 p-FETs with Chemically Doped Contacts. *Nano Lett.* **2012**, *12*, 3788–3792.
14. Lee, Y.-H.; Yu, L.; Wang, H.; Fang, W.; Ling, X.; Shi, Y.; Lin, C.-T.; Huang, J.-K.; Chang, M.-T.; Chang, C.-S.; *et al.* Synthesis and Transfer of Single-Layer Transition Metal Disulfides on Diverse Surfaces. *Nano Lett.* **2013**, *13*, 1852–1857.
15. Zhang, W.; Chuu, C.-P.; Huang, J.-K.; Chen, C.-H.; Tsai, M.-L.; Chang, Y.-H.; Liang, C.-T.; Chen, Y.-Z.; Chueh, Y.-L.; He, J.-H.; *et al.* Ultrahigh-Gain Photodetectors Based on Atomically Thin Graphene-MoS_2 Heterostructures. *Sci. Rep.* **2014**, *4*, 3826.
16. Bertolazzi, S.; Krasnozhon, D.; Kis, A. Nonvolatile Memory Cells Based on MoS_2/Graphene Heterostructures. *ACS Nano* **2013**, *7*, 3246–3252.
17. Britnell, L.; Gorbachev, R. V.; Jalil, R.; Belle, B. D.; Schedin, F.; Mishchenko, A.; Georgiou, T.; Katsnelson, M. I.; Eaves, L.; Morozov, S. V.; *et al.* Field-Effect Tunneling Transistor Based on Vertical Graphene Heterostructures. *Science* **2012**, *335*, 947–950.
18. Geim, A. K.; Grigorieva, I. V. Van der Waals Heterostructures. *Nature* **2013**, *499*, 419–425.
19. Sup Choi, M.; Lee, G.-H.; Yu, Y.-J.; Lee, D.-Y.; Hwan Lee, S.; Kim, P.; Hone, J.; Jong Yoo, W. Controlled Charge Trapping by Molybdenum Disulphide and Graphene in Ultrathin Heterostructured Memory Devices. *Nat. Commun.* **2013**, *4*, 1624.
20. Georgiou, T.; Jalil, R.; Belle, B. D.; Britnell, L.; Gorbachev, R. V.; Morozov, S. V.; Kim, Y.-J.; Gholinia, A.; Haigh, S. J.; Makarovsky, O.; *et al.* Vertical Field-effect Transistor based on Graphene-WS_2 Heterostructures for Flexible and Transparent Electronics. *Nat. Nanotechnol.* **2013**, *8*, 100–103.
21. Britnell, L.; Ribeiro, R. M.; Eckmann, A.; Jalil, R.; Belle, B. D.; Mishchenko, A.; Kim, Y.-J.; Gorbachev, R. V.; Georgiou, T.; Morozov, S. V.; *et al.* Strong Light-Matter Interactions in Heterostructures of Atomically Thin Films. *Science* **2013**, *340*, 1311–1314.
22. Haigh, S. J.; Gholinia, A.; Jalil, R.; Romani, S.; Britnell, L.; Elias, D. C.; Novoselov, K. S.; Ponomarenko, L. A.; Geim, A. K.; Gorbachev, R. Cross-sectional Imaging of Individual Layers and Buried Interfaces of Graphene-based Heterostructures and Superlattices. *Nat. Mater.* **2012**, *11*, 764–767.
23. Rivera, P.; Schaibley, J. R.; Jones, A. M.; Ross, J. S.; Wu, S.; Aivazian, G.; Klement, P.; Ghimire, N. J.; Yan, J.; Mandrus, D. G.; *et al.* Observation of Long-Lived Interlayer Excitons in Monolayer $MoSe_2$-WSe_2 Heterostructures. 2014, ArXiv:1403.4985. arXiv.org e-Print arXiv. http://arxiv.org/abs/1403.4985.
24. Cheng, R.; Li, D.; Zhou, H.; Wang, C.; Yin, A.; Jiang, S.; Liu, Y.; Chen, Y.; Huang, Y.; Duan, X. Electroluminescence and Photocurrent Generation from Atomically Sharp WSe_2/MoS_2 Heterojunction p-n Diodes. 2014, ArXiv:1403.3447. arXiv.org e-Print arXiv. http://arxiv.org/abs/1403.3447.
25. Furchi, M. M.; Pospischil, A.; Libisch, F.; Burgdorfer, J.; Mueller, T. Photovoltaic Effect in an Electrically Tunable van der Waals Heterojunction. 2014, ArXiv:1403.2652. arXiv.org e-Print arXiv. http://arxiv.org/abs/1403.2652.
26. Lee, C.-H.; Lee, G.-H.; van der Zande, A. M.; Chen, W.; Li, Y.; Han, M.; Cui, X.; Arefe, G.; Nuckolls, C.; Heinz, T. F.; *et al.* Atomically Thin *p-n* Junctions with van der Waals Heterointerfaces. *Nat. Nanotechnol.* **2014**, *9*, 676–681.
27. Fang, H.; Battaglia, C.; Carraro, C.; Nemsak, S.; Ozdol, B.; Kang, J. S.; Bechtel, H. A.; Desai, S. B.; Kronast, F.; Unal, A. A.; *et al.* Strong Interlayer Coupling in van der Waals Heterostructures Built from Single-Layer Chalcogenides. *Proc. Natl. Acad. Sci. U.S.A.* **2014**, *111*, 6198–6202.
28. Zhang, C.; Johnson, A.; Hsu, C. L.; Li, L. J.; Shih, C. K. Direct Imaging of Band Profile in Single Layer MoS_2 on Graphite: Quasiparticle Energy Gap, Metallic Edge States, and Edge Band Bending. *Nano Lett.* **2014**, *14*, 2443–2447.
29. Luo, X.; Zhao, Y.; Zhang, J.; Toh, M.; Kloc, C.; Xiong, Q.; Quek, S. Y. Effects of lower symmetry and dimensionality on Raman spectra in two-dimensional WSe_2. *Phys. Rev. B* **2013**, *88*, 195313.
30. Tonndorf, P.; Schmidt, R.; Böttger, P.; Zhang, X.; Börner, J.; Liebig, A.; Albrecht, M.; Kloc, C.; Gordan, O.; Zahn, D. R. T.; *et al.* Photoluminescence Emission and Raman Response of Monolayer MoS_2, $MoSe_2$, and WSe_2. *Opt. Express* **2013**, *21*, 4908–4916.
31. Molina-Sánchez, A.; Wirtz, L. Phonons in Single-Layer and Few-Layer MoS_2 and WS_2. *Phys. Rev. B* **2011**, *84*, 155413.
32. Wieting, T. J.; Verble, J. L. Infrared and Raman Studies of Long-Wavelength Optical Phonons in Hexagonal MoS_2. *Phys. Rev. B* **1971**, *3*, 4286–4292.
33. Rice, C.; Young, R. J.; Zan, R.; Bangert, U.; Wolverson, D.; Georgiou, T.; Jalil, R.; Novoselov, K. S. Raman-Scattering Measurements and First-Principles Calculations of Strain-induced Phonon Shifts in Monolayer MoS_2. *Phys. Rev. B* **2013**, *87*, 081307.
34. Li, H.; Zhang, Q.; Yap, C. C. R.; Tay, B. K.; Edwin, T. H. T.; Olivier, A.; Baillargeat, D. From Bulk to Monolayer MoS_2: Evolution of Raman Scattering. *Adv. Funct. Mater.* **2012**, *22*, 1385–1390.
35. Terrones, H.; Corro, E. D.; Feng, S.; Poumirol, J. M.; Rhodes, D.; Smirnov, D.; Pradhan, N. R.; Lin, Z.; Nguyen, M. A. T.; Elias, A. L.; *et al.* New First Order Raman-active Modes in Few Layered Transition Metal Dichalcogenides. *Sci. Rep.* **2014**, *4*, 4215.
36. Zhang, X.; Han, W. P.; Wu, J. B.; Milana, S.; Lu, Y.; Li, Q. Q.; Ferrari, A. C.; Tan, P. H. Raman Spectroscopy of Shear and Layer Breathing Modes in Multilayer MoS_2. *Phys. Rev. B* **2013**, *87*, 115413.
37. Zhao, W.; Ghorannevis, Z.; Amara, K. K.; Pang, J. R.; Toh, M.; Zhang, X.; Kloc, C.; Tan, P. H.; Eda, G. Lattice Dynamics in Mono- and Few-layer Sheets of WS_2 and WSe_2. *Nanoscale* **2013**, *5*, 9677–9683.
38. Clark, S. J.; Segall, M. D.; Pickard, C. J.; Hasnip, P. J.; Probert, M. J.; Refson, K.; Payne, M. C. First Principles Methods using CASTEP. *Z. Kristallogr.* **2005**, *220*, 567–570.
39. Ortmann, F.; Bechstedt, F.; Schmidt, W. G. Semiempirical van der Waals Correction to the Density Functional Description of Solids and Molecular Structures. *Phys. Rev. B* **2006**, *73*, 205101.
40. Refson, K.; Tulip, P. R.; Clark, S. J. Variational Density-Functional Perturbation Theory for Dielectrics and Lattice Dynamics. *Phys. Rev. B* **2006**, *73*, 155114.
41. Wang, Y.; Cong, C.; Qiu, C.; Yu, T. Raman Spectroscopy Study of Lattice Vibration and Crystallographic Orientation of Monolayer MoS_2 under Uniaxial Strain. *Small* **2013**, *9*, 2857–2861.
42. Castellanos-Gomez, A.; Roldán, R.; Cappelluti, E.; Buscema, M.; Guinea, F.; van der Zant, H. S. J.; Steele, G. A. Local Strain Engineering in Atomically Thin MoS_2. *Nano Lett.* **2013**, *13*, 5361–5366.
43. Zhu, C. R.; Wang, G.; Liu, B. L.; Marie, X.; Qiao, X. F.; Zhang, X.; Wu, X. X.; Fan, H.; Tan, P. H.; Amand, T.; *et al.* Strain Tuning of Optical Emission Energy and Polarization in Monolayer and Bilayer MoS_2. *Phys. Rev. B* **2013**, *88*, 121301.

44. Shi, Y.; Huang, J.-K.; Jin, L.; Hsu, Y.-T.; Yu, S. F.; Li, L.-J.; Yang, H. Y. Selective Decoration of Au Nanoparticles on Monolayer MoS_2 Single Crystals. *Sci. Rep.* **2013**, *3*, 1839.
45. Chakraborty, B.; Bera, A.; Muthu, D. V. S.; Bhowmick, S.; Waghmare, U. V.; Sood, A. K. Symmetry-dependent Phonon Renormalization in Monolayer MoS_2 transistor. *Phys. Rev. B* **2012**, *85*, 161403.
46. Liu, K.; Zhang, L.; Cao, T.; Jin, C.; Qiu, D.; Zhou, Q.; Zettl, A.; Yang, P.; Louie, S. G.; Wang, F. Evolution of Interlayer Coupling in Twisted MoS_2 Bilayers. *ArXiv* **2014**, *1406*, 6487.
47. van der Zande, A. M.; Kunstmann, J.; Chernikov, A.; Chenet, D. A.; You, Y.; Zhang, X.; Huang, P. Y.; Berkelbach, T. C.; Wang, L.; Zhang, F.; *et al.* Tailoring the Electronic Structure in Bilayer Molybdenum Disulfide *via* Interlayer Twist. *Nano Lett.* **2014**, *14*, 3869–3875.
48. Chiu, M.-H.; Zhang, C.; Shiu, H. W.; Chuu, C.-P.; Chen, C.-H.; Chang, C.-Y. S.; Chen, C.-H.; Chou, M.-Y.; *et al.* Determination of Band Alignment in Transition Metal Dichalcogenides Heterojunctions. *ArXiv* **2014**, *1406*, 5137.
49. Ramasubramaniam, A. Large Excitonic effect in Monolayer of Molybdenum and Tungsten Dichalcogenides. *Phys. Rev. B* **2012**, *86*, 115409.
50. Klots, A. R.; Newaz, A. K. M.; Wang, B.; Prasai, D.; Krzyzanowska, H.; Caudel, D.; Ghimire, N. J.; Yan, J.; Ivanov, B. L.; Velizhanin, K. A.; *et al.* Probing Excitonic States in Ultraclean Suspended Two-dimensional Semiconductors by Photocurrent Spectroscopy. 2014, ArXiv:1403.6455. arXiv.org e-Print arXiv. http://arxiv-web3.library.cornell.edu/abs/1403.6455v1.
51. Shi, H.; Pan, H.; Zhang, Y.-W.; Yakobson, B. I. Quasiparticle Band Structures and Optical Properties of Strained Monolayer MoS_2 and WS_2. *Phys. Rev. B* **2013**, *87*, 155304.
52. Liang, Y.; Huang, S.; Soklaski, R.; Yang, L. Quasiparticle Band-edge Energy and Band Offsets of Monolayer of Molybdenum and Tungsten Chalcogenides. *Appl. Phys. Lett.* **2013**, *103*, 042106.
53. Su, S.-H.; Hsu, W.-T.; Hsu, C.-L.; Chen, C.-H.; Chiu, M.-H.; Lin, Y.-C.; Chang, W.-H.; Suenaga, K.; He, J.-H.; Li, L.-J. Controllable Synthesis of Band Gap-Tunable and Monolayer Transition Metal Dichalcogenide Alloys. *Front. Energy Res.* **2014**, *2*, 27.
54. Ceperley, D. M.; Alder, B. J. Ground-State of The Electron-Gas by a Stochastic Method. *Phys. Rev. Lett.* **1980**, *45*, 566–569.
55. Perdew, J. P.; Zunger, A. Self-Interaction Correction to Density-Functional Approximations for Many-Electron Systems. *Phys. Rev. B* **1981**, *23*, 5048–5079.
56. Ding, Y.; Wang, Y.; Ni, J.; Shi, L.; Shi, S.; Tang, W. First Principles Study of Structural, Vibrational and Electronic Properties of Graphene-like MX_2 (M = Mo, Nb, W, Ta; X = S, Se, Te) Monolayers. *Physica B* **2011**, *406*, 2254–2260.
57. Mahatha, S. K.; Patel, K. D.; Menon, K. S. R. Electronic Structure Investigation of MoS_2 and $MoSe_2$ using Angle-resolved Photoemission Spectroscopy and *ab Initio* Band Structure Studies. *J. Phys.: Condens. Matter* **2012**, *24*, 475504.
58. Perdew, J. P.; Chevary, J. A.; Vosko, S. H.; Jackson, K. A.; Pederson, M. R.; Singh, D. J.; Fiolhais, C. Atoms, Molecules, Solids, And Surfaces: Applications of the Generalized Gradient Approximation for the Exchange and Correlation. *Phys. Rev. B* **1992**, *46*, 6671–6687.
59. Terrones, H.; Lopez-Urias, F.; Terrones, M. Novel Hetero-Layered Materials with Tunable Direct Band Gaps by Sandwiching Different Metal Disulfides and Diselenides. *Sci. Rep.* **2013**, *3*, 1549.